The Response of Balanced Hurricanes to Local Sources of Heat and Momentum

LLOYD J. SHAPIRO AND HUGH E. WILLOUGHBY

National Hurricane Research Laboratory, Atlantic Oceanographic and Meteorological Laboratories, NOAA, Coral Gables, FL 33146

(Manuscript received 26 May 1981, in final form 28 September 1981)

ABSTRACT

Eliassen's (1951) diagnostic technique is used to calculate the secondary circulation induced by point sources of heat and momentum in balanced, hurricane-like vortices. Scale analysis reveals that such responses are independent of the horizontal scale of the vortex. Analytic solutions for the secondary circulation are readily obtained in idealized barotropic vortices, but numerical methods are required for more realistic barotropic and baroclinic vortices. For sources near the radius of maximum wind, the local, two-dimensional, streamfunction dipole response of Eliassen is modified by both the spatial variations of the vortex structure and the influences of boundary conditions.

The secondary flow advects mean-flow buoyancy and angular momentum and thus leads to a slow evolution of the vortex structure. In weak systems (maximum tangential wind < 35 m s^{-1}), the restraining influences of structure and boundaries lengthen the time scale of the vortex evolution. In stronger vortices, the horizontal scale of the response is smaller; the restraining influences are less important, and the evolution is faster. When the maximum wind exceeds 35 m s^{-1}, recirculation of air within the vortex core tends to form an eye.

The most rapid temporal changes in tangential wind lie inside the eye, where the horizontal gradients of angular momentum are strongest. In most cases, the tangential wind increases most rapidly just inside the radius of maximum wind and decreases near the central axis of the vortex. This effect leads to contraction of the wind maximum as the vortex intensifies. The present results are compared with observations and other theoretical results.

1. Introduction

Eliassen (1951) first treated the gradual response of a balanced, symmetric vortex to imposed sources of heat or momentum. Willoughby (1979, hereafter abbreviated as FC) used Eliassen's technique to diagnose the transverse circulation induced by parameterized convective forcing in hurricanes. Other investigators, cited in FC, have also applied Eliassen's method to the hurricane problem. Recently, Challa and Pfeffer (1980) used the balanced, prognostic model of Sundqvist (1970) to investigate the role of imposed momentum fluxes in hurricane intensification. Smith (1981) also treats the secondary circulation problem in the context of balanced single- and multi-layer models based on the shallow-water approximation.

In Eliassen (1951) the principal part of the Green's function solutions for unit point sources were obtained. These solutions are locally valid two-dimensional dipoles. Since the response to any arbitrary forcing can be represented as a superposition of Green's functions, this approach gives valuable insight into the changing character of the response as the structure and intensity of a vortex vary.

The simple dipole character of the solutions will be altered significantly by both the spatial variation of the vortex structure and the boundary conditions. For example, an axisymmetric solution can have no radial flow across the vortex axis. This and other effects lead to dramatic changes in the response when the locally valid dipole ceases to represent the complete solution. This paper generalizes Eliassen's local analysis to hurricane-like vortices of finite extent.

In the next section we reexamine the scaling argument of FC and show that the behavior of the symmetric hurricane vortex is independent of its horizontal spatial scale, provided the Rossby number is large. In Section 3 the responses of barotropic vortices to point sources of heat and momentum are evaluated. Both idealized vortices amenable to analytic solutions and more realistic ones requiring numerical solutions are treated. In Section 4 we use the numerical model of FC to extend the analysis to more realistic baroclinic vortices. Both the strength of the vortices and the height and radius of the source's location are varied. Section 5 summarizes and interprets the results.

2. Formulation

In FC both horizontal and vertical lengths were scaled with the radius of the eye (15 km), giving an aspect ratio of 1. Velocities were scaled with the

maximum tangential wind present in the storm. Then, following conventional treatments of planetary-scale circulations (e.g., Holton, 1975), the motions were described as a slowly evolving, symmetric vortex on which both a symmetric secondary circulation and a spectrum of propagating asymmetric waves were superimposed. Much of the formulation of FC arose from interest in asymmetric features of very intense hurricanes, so the aspect ratio and Froude number were fixed at unity, while the buoyancy was scaled with the vertical acceleration. The present scaling keeps the same methodology and the same scaling for wind speed and horizontal lengths, but differs in that the aspect ratio and Froude number appear explicitly and are generally less than one. Buoyancy is here scaled hydrostatically with the vertical gradient of geopotential, rather than with the acceleration of the vertical wind. These changes do not significantly alter the form of the equations, but do greatly extend the range of their validity. The variables used are as follows:

$r = Rr^*$	radius
$z = Zz^*$	vertical, log-pressure coordinate
λ	azimuth
$t = (R/V)t^*$	time
$u = Uu^*$	radial wind velocity
$v = Vv^*$	tangential wind velocity
$w = Ww^*$	vertical wind velocity
$\phi = (\mu gH)\phi^*$	geopotential
$b = (\mu gH/Z)b^*$	buoyancy
$\rho(z) = (1.1 \text{ kg m}^{-3})\rho^*(z^*)$	background density
$H = (Z/2)H^*$	density scale height
$N = \mathbf{N}N^*$	buoyancy (Brunt-Väisälä) frequency
f	Coriolis frequency
$g = (V^2/R)g^*$	gravitational acceleration
$\zeta = \frac{V}{R}\left(\frac{\partial v^*}{\partial r^*} + \frac{v^*}{r^*} + \frac{1}{\text{Ro}}\right) = \frac{V}{R}\zeta^*$	absolute vorticity
$\xi = \frac{V}{R}\left(\frac{2v^*}{r^*} + \frac{1}{\text{Ro}}\right) = \frac{V}{R}\xi^*$	inertia parameter
$S = \frac{V}{Z}\frac{\partial v^*}{\partial z^*} = \frac{V}{Z}S^*$	vertical shear
$\text{Ro} = V/fR$	Rossby number
$\text{Fr} = V^2/(\mu gH)$	Froude number
$A^* = Z/R$	aspect ratio
$\epsilon = U/V$	tangent of the angle between the horizontal wind and a circle about the origin
$\text{Ri} = (\mathbf{N}Z/V)^2$	Richardson number
$X\Phi_x$	dimensional forcing of the dependent variable x, where x may be u, v, w or b. Φ_x by itself is the nondimensional forcing.

Here the starred variables denote the nondimensional equivalents of the unstarred ones, and capital letters denote scale factors.

As in FC, the horizontal spatial scale is chosen to be the radius of maximum wind ($R = r_{\max}$); the vertical scale (Z = 15 km) is the depth of the troposphere, but these scales are not constrained to be the same. Mass continuity requires $W = A^*U$. The quantity μ may be interpreted as either the ratio of the displacement of a constant-pressure surface to the scale height or the ratio of the storm's surface pressure anomaly to the total surface pressure. Table 1 shows typical values of the scaling parameters for five data sets from recent Atlantic hurricanes. The values of ϵ shown in Table 1 are estimated from the maximum observed azimuthal mean updraft for each storm and the relation $\epsilon = W/(VA^*)$.

In nondimensional form, with terms of order two and higher in ϵ omitted, the governing equations are

$$\epsilon\left(\frac{\partial u^*}{\partial t^*} + \frac{v^*}{r^*}\frac{\partial u^*}{\partial \lambda}\right) - v^*\left(\frac{v^*}{r^*} + \frac{1}{\text{Ro}}\right) + \frac{1}{\text{Fr}}\frac{\partial \phi^*}{\partial r^*} = \epsilon\Phi_u, \quad (1.1)$$

TABLE 1. The scaling parameters determined from seven sets of data observed by research aircraft in recent hurricanes.

Storm	Date	V (m s^{-1})	R (km)	A^*	μ	ϵ	Ro	Ri	Fr
Anita	2 Sep 1977	62	23	0.65	0.08	0.025	44.6	12.7	0.65
David	30 Aug 1979	50	14	1.07	0.07	0.075	87.0	19.6	0.49
David	31 Aug 1979	60	23	0.65	0.09	0.1	61.0	13.6	0.56
David	2 Sep 1979	18	37	0.41	0.01	0.14	8.9	151.2	0.34
Frederic	11 Sep 1979	29	66	0.23	0.02	0.15	6.7	58.3	0.71
Allen	5 Aug 1980	64	38	0.41	0.08	0.1	41.4	12.0	0.68
Allen	8 Aug 1980	59	16	0.94	0.07	0.04	66.6	14.1	0.63

$$\frac{\partial v^*}{\partial t^*} + \frac{v^*}{r^*}\frac{\partial v^*}{\partial \lambda} + \epsilon(u^*\zeta^* + w^*S^*) + \frac{1}{\mathrm{Fr}}\frac{1}{r^*}\frac{\partial \phi^*}{\partial \lambda} = \Phi_v, \quad (1.2)$$

$$\epsilon A^{*2}\left(\frac{\partial w^*}{\partial t^*} + \frac{v^*}{r^*}\frac{\partial w^*}{\partial \lambda}\right) + \frac{1}{\mathrm{Fr}}\left(-b^* + \frac{\partial \phi^*}{\partial z^*}\right) = \epsilon\Phi_w, \quad (1.3)$$

$$\frac{1}{\mathrm{Fr}}\left(\frac{\partial b^*}{\partial t^*} + \frac{v^*}{r^*}\frac{\partial b^*}{\partial \lambda} + \epsilon u^*\frac{\partial b^*}{\partial r^*}\right) + \epsilon \mathrm{Ri} N^{*2} w^* = \Phi_b, \quad (1.4)$$

$$\epsilon\left(\frac{\partial u^*}{\partial r^*} + \frac{u^*}{r^*} + \frac{\partial w^*}{\partial z^*} - \frac{2w^*}{H^*}\right) + \frac{1}{r^*}\frac{\partial v^*}{\partial \lambda} = 0. \quad (1.5)$$

As in FC, ϵ characterizes the ratio of the radial, vertical, and asymmetric tangential velocities to the symmetric tangential (swirling) velocity. The essential observation on which the scaling is based is that ϵ is small in the free atmosphere and the symmetric vortex evolves on a time scale appropriate to radial or vertical advection, whereas the asymmetric flow evolves on the more rapid time scale for tangential advection. This condition is expressed as

$$\left.\begin{aligned} u^* &= u_s^*(r^*, z^*, \epsilon t^*) + u_a^*(r^*, z^*, \lambda, t^*) + \epsilon(\cdots \\ v^* &= v_s^*(r^*, z^*, \epsilon t^*) + \epsilon v_a^*(r^*, z^*, \lambda, t^*) + \epsilon^2(\cdots \\ w^* &= w_s^*(r^*, z^*, \epsilon t^*) + w_a^*(r^*, z^*, \lambda, t^*) + \epsilon(\cdots \\ b^* &= b_s^*(r^*, z^*, \epsilon t^*) + \epsilon b_a^*(r^*, z^*, \lambda, t^*) + \epsilon^2(\cdots \\ \phi^* &= \phi_s^*(r^*, z^*, \epsilon t^*) + \epsilon\phi_a^*(r^*, z^*, \lambda, t^*) + \epsilon^2(\cdots \end{aligned}\right\}. \quad (2)$$

Here the subscripts s and a denote the symmetric and asymmetric parts of the nondimensional variables. In addition, the nondimensional forcings on the right-hand side of (1.1)–(1.5) are required to match the time scales of the respective dependent variables. In (3), for example, ϵ multiplies Δv_s^*, the forced change in v_s^*, so that the change matches the slow time scale appropriate to v_s^* itself. These considerations lead to the following representations for the forcings:

$$\left.\begin{aligned} \epsilon\Phi_u &= \frac{\epsilon}{\tau^*}(\epsilon\Delta u_s^* + \Delta u_a^*) \\ \Phi_v &= \frac{\epsilon}{\tau^*}(\Delta v_s^* + \Delta v_a^*) \\ \epsilon\Phi_w &= \frac{\epsilon}{\tau^*}(\epsilon\Delta w_s^* + \Delta w_a^*) \\ \Phi_b &= \frac{\epsilon g^*}{\tau^*}(\Delta T_s + \Delta T_a)/T. \end{aligned}\right\}. \quad (3)$$

Here τ is the dimensional time scale of the forcing, $\tau^* = \epsilon V\tau/R$. ΔT_s and ΔT_a are the temperature changes, due to symmetric and asymmetric heating respectively, and T is the variable background temperature. All the quantities in parentheses in (3) represent the changes in the variables that would result if the forcing acted through time τ without any compensating secondary flow.

If (2) and (3) are substituted into (1.1)–(1.5) and all terms of second order and higher are discarded, then collection of the zero-order terms in (1.1) and (1.3) and azimuthal averaging of the first-order terms in (1.2), (1.4), and (1.5) yields a set of equations for the symmetric motions:

$$v_s^*\left(\frac{v_s^*}{r^*} + \frac{1}{\mathrm{Ro}}\right) = \frac{1}{\mathrm{Fr}}\frac{\partial \phi_s^*}{\partial r^*}, \quad (4.1)$$

$$\frac{\partial v_s^*}{\partial t^*} + u_s^*\zeta_s^* + w_s^*S_s^* = \mathbf{V}_s^*, \quad (4.2)$$

$$\frac{\partial \phi_s^*}{\partial z^*} = b_s^*, \quad (4.3)$$

$$\frac{1}{\mathrm{Fr}}\frac{\partial b_s^*}{\partial t^*} + u_s^*\xi_s^*S_s^* + \mathrm{Ri}N^{*2}w_s^* = \mathbf{B}_s^*, \quad (4.4)$$

$$\frac{\partial u_s^*}{\partial r^*} + \frac{u_s^*}{r^*} + \frac{\partial w_s^*}{\partial z^*} - \frac{2w_s^*}{H^*} = 0. \quad (4.5)$$

In (4.4) the identity $\partial b_s^*/\partial r^* = \mathrm{Fr}\xi_s^*S_s^*$ is used.

In the interest of both simplicity and consistency with FC, boldfaced $\mathbf{V}_s^*$ and $\mathbf{B}_s^*$ are used to represent the momentum and buoyancy sources in the symmetric equations. The second-order eddy correlation terms that were discarded in the derivation of (4.2) and (4.4) can be incorporated into $\mathbf{V}_s^*$ and $\mathbf{B}_s^*$. In the boundary layer, the $\partial(u^{*2}/2)/\partial r^*$ term that was neglected in (1.1) can be of first order. This leads to a correction of the gradient wind. This correction is not crucial for the present analysis since the effects that we are considering are superposed upon the frictional response. In a prognostic model, however, the corrected frictional convergence would change the long-term evolution of the storm. The first-order terms in (1.1) and (1.3) and the terms left after subtraction of (4.2), (4.4) and (4.5) from the first-order terms of (1.2), (1.4) and (1.5) provide the governing equations for the asymmetric motions. Aside from the explicit appearance of A^* and Fr, these equations are virtually identical to (10) of FC and are not displayed here.

It is remarkable that the scaling of (4.1)–(4.5) depends only upon the Froude, Richardson and Rossby numbers, and does not involve the aspect ratio. Table 1 shows that, aside from weak, poorly-organized systems such as Hurricane David on 2 September 1979, a single value of Fr between 0.5 and 1.0 may be appropriate. Although Ro is proportional to the maximum wind speed, it is large and appears only as a reciprocal, so the solutions are insensitive to its exact value. Ri depends explicitly on the inverse square of the wind speed. Since the depth of the troposphere and the buoyancy frequency are both observed to be nearly constant, Ri is a measure of the hurricane's intensity. It is also the only parameter of (4.1)–(4.5) that both influences the solutions significantly and changes in value from case to case. Thus, both the role of Ri and the absence of A^* combine to make the nondimensional symmetric response in all hurricanes of a given wind speed identical regardless of the storm's horizontal scale.

The asymmetric equations, however, do contain A^*. Interactions between the symmetric and asymmetric motions (e.g., Willoughby, 1978) may then cause storms of differing horizontal scale to have radically different structure even in the azimuthal mean. It is, nevertheless, significant that the symmetric response of a hurricane to a given heat or momentum source depends only upon the character of the source and the storm's intensity and not upon the storm's horizontal scale.

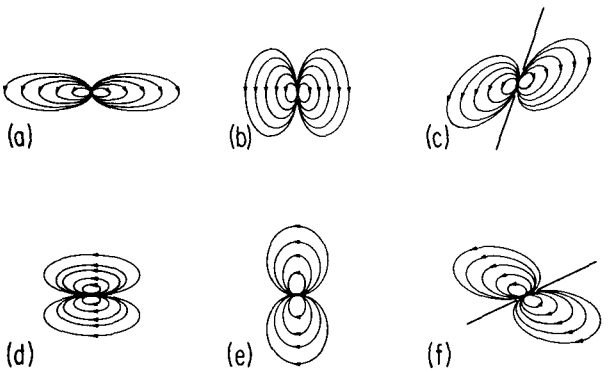

FIG. 1. Streamfunction responses to point sources of: (a) Heat in a barotropic vortex with weak inertial stability ($R^* > 1$), (b) heat in a barotropic vortex with strong inertial stability, (c) heat in a baroclinic vortex, (d) momentum in a barotropic vortex with weak inertial stability, (e) momentum in a barotropic vortex with strong inertial stability, and (f) momentum in a baroclinic vortex. [Based on Figs. 8, 9, 11, and 12 of Eliassen, (1951).]

Since our attention will be confined to symmetric motions for the remainder of this paper, we will drop the subscript s when we refer to such motions. Henceforth u and u^* will be the dimensional and nondimensional azimuthal mean radial wind, respectively, and similarly for the other variables.

The tangential momentum (4.2) and buoyancy (4.4) equations are combined, following Eliassen (1951), to yield a diagnostic expression for the streamfunction of the symmetric motions in the r–z plane:

$$\frac{\partial}{\partial r^*}\left(\frac{\mathrm{Ri}N^{*2}}{r^*\rho^*}\frac{\partial\psi}{\partial r^*} - \frac{S^*\xi^*}{r^*\rho^*}\frac{\partial\psi}{\partial z^*}\right) + \frac{\partial}{\partial z^*}\left(\frac{\zeta^*\xi^*}{r^*\rho^*}\frac{\partial\psi}{\partial z^*} - \frac{S^*\xi^*}{r^*\rho^*}\frac{\partial\psi}{\partial r^*}\right) = -\frac{\partial}{\partial z^*}(\xi^*\mathbf{V}^*) + \frac{\partial}{\partial r^*}\mathbf{B}^*, \quad (5)$$

where $u^* = -(1/r^*\rho^*)(\partial\psi/\partial z^*)$ and $w^* = (1/r^*\rho^*)(\partial\psi/\partial r^*)$.

This equation is elliptic, and the vortex is stable, as long as the discriminant

$$D^* \equiv \mathrm{Ri}N^{*2}\zeta^*\xi^* - (S^*\xi^*)^2 > 0. \quad (6)$$

When $D^* < 0$ the vortex is subject to symmetric instability (e.g., Ooyama, 1966). We shall consider stable vortices only. In this case, D^* is a measure of the combined inertial and buoyant resistance to forced secondary motions.

In Eliassen's (1951) original paper, the responses to point sources—i.e., azimuthal rings of heating and tangential momentum addition—were treated extensively. Examples of his solutions are shown schematically in Fig. 1. The flow through the heat source itself follows a (nearly vertical) surface of constant angular momentum; that for a momentum source follows a (nearly horizontal) isentropic surface. For sources of heat and momentum the sense of the flow

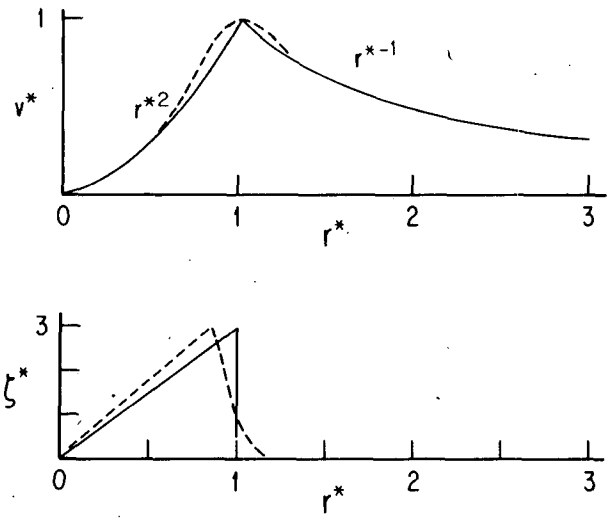

FIG. 2: Dependence of nondimensional tangential velocity v^*, and vorticity ζ^*, on radius r^* for idealized barotropic vortex used in computing analytic solutions (solid lines) and numerical solutions (dashed lines).

is upward and outward, respectively; for sinks the flow is reversed. The center of the vortex lies to the left in this figure. In the warm-core system of Figs. 1c and 1f, the warm anomaly that supports the slope of the constant momentum and entropy surfaces increases toward the upper left.

If the coefficients in (5) vary slowly over the domain and the forcing is remote from the boundaries, the elliptical streamline patterns expand horizontally when $\zeta^*\xi^*$ decreases relative to $\mathrm{Ri}N^{*2}$ and contract when it increases. The local, nondimensional Rossby radius of deformation,

$$R^* \equiv \left(\frac{\mathrm{Ri}N^{*2}}{\zeta^*\xi^*}\right)^{1/2}, \tag{7}$$

is a measure of this tendency. The effects of changes in R^* are illustrated in Fig. 1. Of particular consequence to hurricane dynamics is the extreme reduction in R^* that takes place in an intense hurricane. At wind speeds above 35 m s^{-1}, $R^* < 2$. Thus, the characteristic horizontal scale of compensating subsidence induced by convection becomes comparable to the diameter of the eye. In a spatially inhomogeneous vortex of limited extent, the character of the response is also sensitive to variations of the coefficients in (5) and the proximity of the boundaries. These effects are the basis for much of the following discussion.

3. Barotropic vortex

The purpose of the analysis in this section is to assess the role of inhomogeneities and boundaries in modifying the simple dipole response. The structure of the vortex is chosen so that analytic solutions may first be obtained. These idealized solutions provide valuable insight into the response in more realistic vortices. The source is placed at the radius of maximum wind (RMW). The source height is specified in the middle troposphere, near the level of observed maximum cumulus heating. Numerical solutions are found for the response in a more realistic vortex, and are compared with the analytic solutions. The instantaneous rate of wind increase inside the radius of maximum wind and its dependence on the strength of the vortex are given particular attention. Using the numerical model, the solution is extended to a more general barotropic vortex.

The idealized vortex used for the analytic solutions is barotropic ($S^* = 0$), Boussinesq, and set in a homogeneous background atmosphere ($\rho^* = \rho^*_{00}$). A coordinate transformation $dx^* = r^*dr^*$ is made, so that $x^* = \frac{1}{2}r^{*2}$. Then (5) becomes

$$\frac{\partial}{\partial x^*}\left(\mathrm{Ri}N^{*2}\frac{\partial \psi}{\partial x^*}\right) + \frac{\partial}{\partial z^*}\left(\frac{\zeta^*\xi^*}{2x^*}\frac{\partial \psi}{\partial z^*}\right) = \rho^*_{00}\frac{\partial \mathbf{B}^*}{\partial x^*} - \frac{\rho^*_{00}}{r^*}\frac{\partial(\xi^*\mathbf{V})}{\partial z^*}. \tag{8}$$

If the vertical stability N^{*2} is constant, and the inertial stability $\zeta^*\xi^*$ is proportional to x^* (or r^{*2}), then the left-hand side of (8) becomes Poisson's equation in Cartesian coordinates (x^*, z^*). $\zeta^*\xi^*/2x^*$ = constant when $v^* + r^*/2\mathrm{Ro}$ equals zero or is proportional to either r^{*2} or r^{*-1}. The radial profiles of v^* and ζ^* constructed from the last two solutions are given by the solid lines in Fig. 2. The nondimensional tangential wind v^* is scaled by the maximum wind $v_{\max}$ at $r = r_m(r^* = 1)$. Since $\mathrm{Ro} \gg 1$, its inverse will be neglected throughout.

With the point source in $r^* < 1$, analytic solutions may be found for the response in that portion of the domain using Eliassen's (1951) solutions and the method of images. The boundary conditions are given in Fig. 3a. The streamfunction is zero at the center of the vortex ($r^* = 0$), the ground ($z^* = 0$) and the tropopause (a lid, $z^* = z^*_T$). In the outer vortex ($r^* > 1$), $\zeta^* = 0$, implying from (8) that $\partial\psi/\partial x^* = w^* = 0$ at the interface $r^* = 1$ and throughout $r^* > 1$. Since the outer vortex is inertially neutral, air may move horizontally there without resistance. The source location is given by $x^* = x^*_0 = \frac{1}{2}r^{*2}_0$, $z^* = z^*_0$. An infinite series of images of equal strength (Figs. 3b and 3c) filling the (x^*, z^*) plane is required to satisfy all boundary conditions on the region $0 \leq r^* \leq 1$, $0 \leq z^* \leq z^*_T$. Only the source and some images that most significantly contribute to the response at $z^* = 0$ are shown. Images at $z^* = -z^*_0$ (not shown), required by the boundary condition at $z^* = 0$, double the horizontal velocity at $z^* = 0$. The image at $r^*_i = (2 - r^{*2}_0)^{1/2}$ is required to satisfy $w^* = 0$ at $r^* = 1$. The images centered on $x^* = -1$ are required to satisfy $u^* = 0$ at $r^* = 0$.

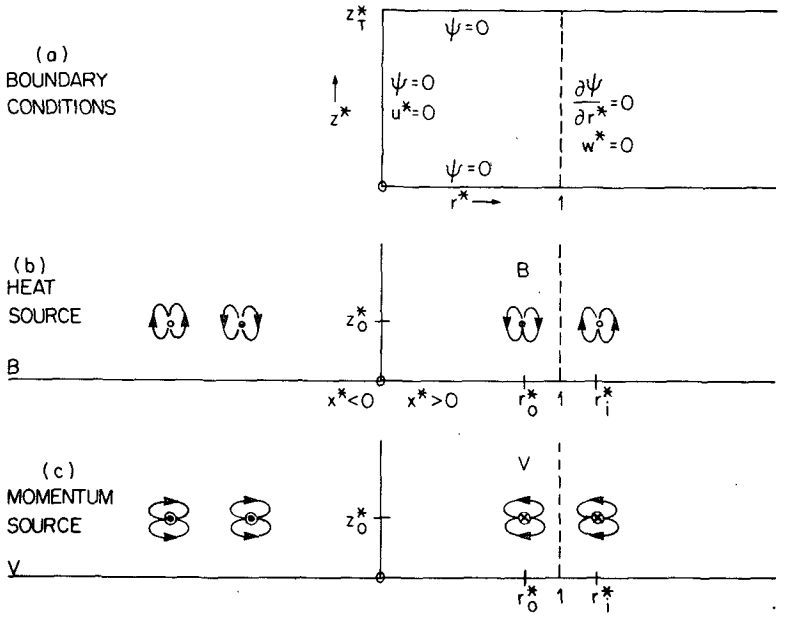

FIG. 3. Geometry and images for analytic solutions: (a) Boundary conditions. (b) Images contributing most significantly to response to heat source **B** at (r_0^*, z_0^*). (c) Same as (b) for momentum source **V**. See text for details.

In the absence of boundaries, Eliassen's (1951) solutions for the principal part of the Green's function for ψ are valid at all points in $0 \leqslant r^* \leqslant 1$, $0 \leqslant z^* \leqslant z_T^*$. For unit point sources of heat and momentum, the nondimensional surface tangential wind tendencies may be computed from Eliassen's solutions [his Eqs. (49) and (51)] and (4.2) applied at $z^* = 0$:

$$\partial v^*/\partial t^*(z^* = 0) = -u^*(z^* = 0)\zeta^*.$$

The dimensional magnitude of the heating in all the following analyses is chosen so that an annular cell of 0.75 km square in the r–z plane would warm at 10°C day^{-1} in the absence of a compensating response. The momentum source is chosen so that the cell would be accelerated at 10 m s^{-1} day^{-1}.[1] Then, the integrated *dimensional* point sources are:

$$\iint \mathbf{B}dxdz = \frac{r_0}{r_m}\frac{g}{T}\frac{\Delta T}{\tau}\Delta r\Delta z,$$

$$\iint \frac{r_m\xi\mathbf{V}}{r}dxdz = \frac{r_0}{r_m}\xi_m\frac{\Delta v}{\tau}\Delta r\Delta z, \qquad (9)$$

where $\Delta T/\tau = 10$°C day^{-1}, $T = 300$°C, $g = 9.8$ m s^{-2}, $\xi_m = \xi(r_m)$, $\Delta v/\tau = 10$ m s^{-1} day^{-1}, and $\Delta r = \Delta z = 0.75$ km.

[1] In a developing hurricane, the *total* thermal and frictional sources have rates of these magnitudes distributed over a volume that encompasses several hundred grid cells. Adjustment of dimensional responses by this factor results in realistic magnitudes (cf. Section 5).

The corresponding dimensional tangential wind tendencies in the absence of boundaries are

$$\frac{\partial v}{\partial t}(z = 0) = \frac{\dfrac{2r_0\gamma^*}{\pi r_m^2 v_{\max}}\dfrac{g}{T}\dfrac{\Delta T}{\tau}\Delta r\Delta z\left(\dfrac{r^2}{r_m^2} - \dfrac{r_0^2}{r_m^2}\right)}{\left[\left(\dfrac{r^2}{r_m^2} - \dfrac{r_0^2}{r_m^2}\right)^2 + \gamma^{*2}\right]^2},$$

(10.1)

$$\frac{\partial v}{\partial t}(z = 0) = \frac{-\dfrac{r_0\gamma^*}{\pi r_m^2 z_0}\dfrac{\Delta v}{\tau}\Delta r\Delta z\left[\left(\dfrac{r^2}{r_m^2} - \dfrac{r_0^2}{r_m^2}\right)^2 - \gamma^{*2}\right]}{\left[\left(\dfrac{r^2}{r_m^2} - \dfrac{r_0^2}{r_m^2}\right)^2 + \gamma^{*2}\right]^2},$$

(10.2)

where

$$\gamma^* = 2\frac{N}{(\xi\xi)_m^{1/2}}\frac{z_0}{r_m} = \left(\frac{2}{3}\right)^{1/2}\frac{Nz_0}{v_{\max}}.$$

γ^* is proportional to the local nondimensional Rossby radius of deformation R^* at r_m, for vertical scale z_0. The dimensional stability N^2 is taken to be 1.0×10^{-4} s^{-2}. In this section the source is at $z_0 = 7.5$ km ($z_0^* = 0.5$), while the lid is at $z_T = 22.5$ km ($z_T^* = 1.5$). Then, with $v_{\max} = 50$ m s^{-1}, $\gamma^* = 1.2$. The parameter γ^* is independent of r_m. Thus, as noted in Section 2, the form of the response is independent of the horizontal scale of the vortex (depending only on $r^* = r/r_m$).

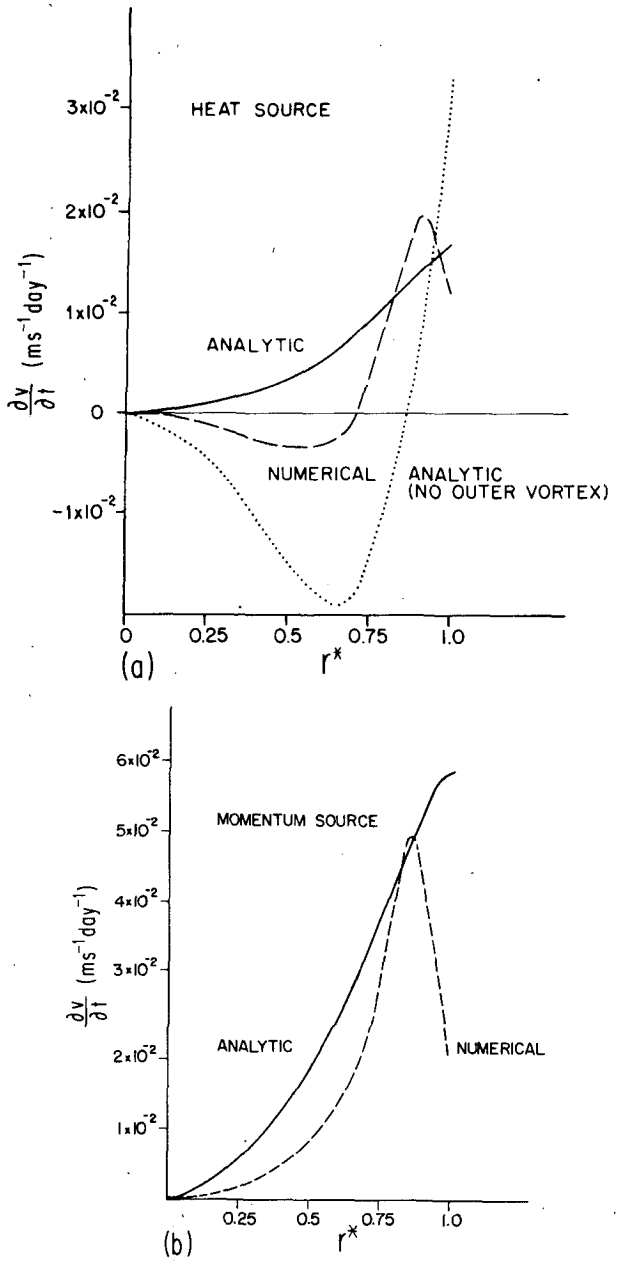

FIG. 4. Dimensional rate of change of surface tangential wind (m s^{-1} day^{-1}) as a function of radius. v_{max} = 50 m s^{-1}. (a) Response to heat source at z_0^* = 0.5, r_0^* = 0.98. Solid line is analytic solution; dashed line is numerical solution. Dotted line is analytic solution in vortex with v^* proportional to r^{*2} in $0 < r^* < \infty$. (b) Response to momentum source at z_0^* = 0.5, r_0^* = 1. Solid line and dashed line are as in (a).

Numerical solutions, corresponding to the analytic ones, are computed. A grid spacing $\Delta r^* = \Delta z^* = 0.05$ is used. Because of finite grid resolution, extended sources that encompass several grid points are used instead of true point sources. The actual sources are square, extending five grid points in both the horizontal and vertical. The maximum input of heat or momentum is at the center point. The source and its first derivatives decrease smoothly to zero around the perimeter of the square. Because the forcing due to heat (momentum) input involves radial (vertical) derivatives of the source, the maximum of $\mathbf{B}_s^*$ ($\mathbf{V}_s^*$) lies to the left and right of (above and below) the center of the source and is zero at the center itself. Thus, the forcing terms on the right-hand side of (8) are nonzero in a region three grid points (0.1 ≡ 1.5 km) square. The magnitude of the integrated nondimensional sources are normalized to unity, so that the dimensional sources are the same as those given in (9).

The vortex is identical to that of the analytic solution, except that a cubic spline transition zone of half-width $3\Delta r^*$ connects the inner ($v^* \propto r^{*2}$) to the outer ($v^* \propto r^{*-1}$) subdomains. The spline is designed to round off the profile of v^* at the peak, while retaining the maximum $v^* = 1$ at $r^* = 1$. The radial profiles of v^* and ζ^* used in the numerical solutions are shown by the dashed lines in Fig. 2. The maximum vorticity is at $r^* = 0.85$. The exact position of the maximum depends on the details of the transition zone. The maximum will always lie in $r^* < 1$ for any smooth wind profile. This vortex is more realistic than that used for the analytic solutions. The numerical solutions are most easily understood, however, in terms of the images used in the analytic formulation. $f \neq 0$ in these solutions, with latitude 20°N. The domain extends to $r^* = 300\Delta r^* = 15$, where $\partial\psi/\partial r^* = 0$ is specified.

The sources for the numerical solutions are centered at radius $r_0^* = 1$ and height $z_0^* = 0.5$. The momentum source ($\mathbf{V}$) for the analytic solutions also is taken at $r_0^* = 1$. Since the image at r_i^* in Fig. 3b counteracts the horizontal flow in $r^* < r_0^*$ due to the heat source ($\mathbf{B}$) at r_0^*, the magnitude of the response in the analytic solution is sensitive to the distance between r_0^* and $r^* = 1$. In the extreme case $r_0^* = 1$, the solution goes to zero. The radius of the heat source for the analytic solutions is taken at $r_0^* = 0.98$, in order to have the magnitude of the response agree with that of the numerical solution. This is necessary because of the sharp transition at $r^* = 1$ between the inner and outer vortex in the analytic formulation. The consequences of this sharp transition will be discussed below.

Radial profiles of $\partial v/\partial t$ at $z^* = 0$ are shown in Figs. 4a and 4b. The analytic solutions (solid lines) are complete, including the source and all images that significantly affect the response. The corresponding numerical solutions are shown by dashed lines. The difference between the numerical and complete analytic solution is due to the transition zone between the inner and outer vortex for the numerical solutions. The numerical solutions for ψ are shown in Figs. 5a and 5b. The nearly inertially neutral outer vortex ($r^* > 1$) allows easy horizontal motion. The

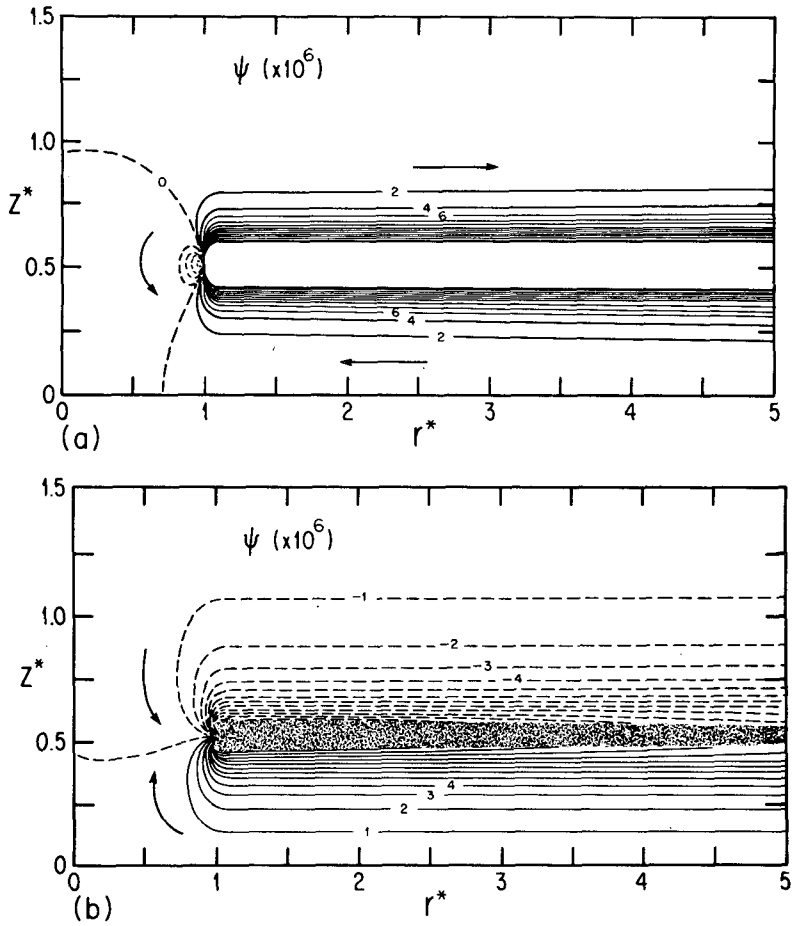

FIG. 5. Numerical solution for mass-flux streamfunction response to sources at $r_0^* = 1$, $z_0^* = 0.5$ in a barotropic vortex. (a) Response to heat source. Contour interval is 2×10^{-6}; each contour unit (1×10^{-6}) is equivalent to 0.825 kg m^{-1} s^{-1}. (b) Response to momentum source. Contour interval is 1×10^{-6}, dimensionally equivalent to 0.825 kg m^{-1} s^{-1}.

vertical motion is essentially confined to $r^* < 1$. The radial gradients of angular momentum are appreciable only in $r^* < 1$. Thus, although u is relatively weak in $r^* < 1$, it can significantly change the tangential winds in that region. The dotted line in Fig. 4a shows the response when the outer, inertially neutral vortex (included in both the numerical and complete analytic solutions) is omitted, and the inner vortex ($v^* \propto r^{*2}$) is allowed to extend to infinity.

The analytic solutions may be used to understand the response to the heat source in Figs. 4a and 5a, obtained from the more realistic numerical formulation. The heat source induces a negative (counterclockwise) gyre in $r^* < r_0^*$. This circulation gives outward flow ($u > 0$) at the surface and results in $\partial v/\partial t < 0$. In the absence of all boundaries, $\partial v/\partial t$ would be <0 throughout $r^* < r_0^*$ [cf. Eq. (10.1)]. At $r^* = r_0^*$, $\partial v/\partial t$ would be zero. The values of $\partial v/\partial t > 0$ near $r^* = 1$ for the dotted line are therefore due to the inner boundary condition $u = 0$ at $r^* = 0$. The image of the source in $x^* < 0$ (Fig. 3b) induces inflow near the ground at $r^* = 1$, so that $\partial v/\partial t > 0$. The vortex used in the numerical solution (dashed line) includes the outer near-inertially neutral vortex in $r^* > 1$. The presence of this outer vortex in the numerical solution leads to tendencies less negative than those for the dotted line, and causes the maximum positive tendency to lie in $r^* < 1$. The former effect may be understood in terms of the images used in computing the complete analytic solution. The outer inertially neutral vortex requires an image source at $r^* = r_i^*$. This image is of the opposite sense to the source at r_0^* (Fig. 3b), and so induces inflow in $r^* < 1$. Thus the outward flow, and negative wind tendencies, in $r^* < 1$ are reduced. The positive tendency is maximum in $r^* < 1$ since the radial profile of v at the RMW is rounded in the numerical formulation, due to the transition zone (Fig. 2). This causes the maximum vorticity, and thus the horizontal advection of angular momentum ($=\partial v/\partial t$), to

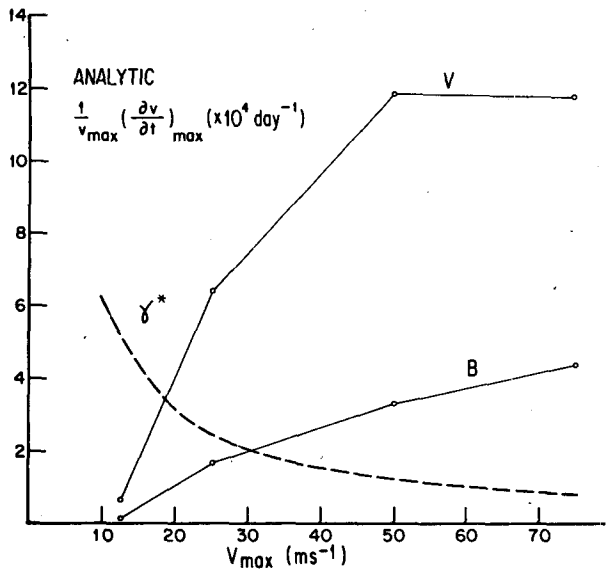

FIG. 6. Rate of intensification of surface tangential wind ($\times 10^4$ day^{-1}) for analytic solutions in idealized barotropic vortices of different strengths. Response to both heat (**B**) and momentum (**V**) sources are shown. Dotted line is analytic solution in vortex with v^* proportional to r^{*2} in $0 < r^* < \infty$. The dashed line shows γ^*, defined in the text.

occur near $r^* = 0.85$. As noted above, the exact position of the maximum depends on the transition zone; but the maximum will occur in $r^* < 1$ for any smooth wind profile. In the complete analytic solution (solid line) the vorticity and thus $\partial v/\partial t$ are maximum at $r^* = 1$. $\partial v/\partial t$ is more positive than for the numerical solution due to the sharp transition at $r^* = 1$ between the inner and outer vortex. The sharper the transition, the stronger the induced inflow in $r^* < 1$.

For the momentum source (Figs. 4b and 5b) the radial flow due to the positive gyre (clockwise) below the source is reinforced by the inertially neutral outer vortex. In terms of the analytic formulation, the image at r_i^* (Fig. 3c) required by the outer vortex is in the same sense as the source at r_0^*. Thus, the flow is inward near the surface, with $\partial v/\partial t > 0$ at all radii. As for the heat source, the maximum of $\partial v/\partial t$ in the numerical solution occurs near $r^* = 0.85$.

Both heat and momentum sources at the RMW intensify the surface vortex [$\partial v/\partial t(r^* = 1) > 0$]. For the more realistic numerical solutions, the angular momentum gradient and $\partial v/\partial t > 0$ are maximum for $r^* < 1$. Thus the RMW tends to move inward as the vortex intensifies. For the momentum source, $\partial v/\partial t > 0$ at all radii. For the heat source (at the given height, in the middle troposphere) the outward advection of angular momentum induces the winds to *decrease* inside $r^* \leq 0.7$ ($u > 0$, $\partial v/\partial t < 0$). As we shall see in the next section, this behavior also is present in a more realistic baroclinic vortex and will tend to make the tangential wind profile concave upward rather than linear in r^*.

The analytic formulation is used to compute the dependence of the maximum surface tangential wind tendency on the strength of the vortex, v_{max}, as shown in Fig. 6. The sources of heat and momentum are kept at the same magnitude and position as above. The tendencies have been converted to normalized rates $(\partial v/\partial t)_{max}/v_{max}$.[2] The most striking feature of the results is the relatively slow response of weaker vortices to both heat and momentum sources. Numerical calculations confirm this result for more realistic vortices. The behavior of the analytic solutions may be easily understood in terms of the constraints imposed by the vortex geometry. As noted previously, these are two: at the center no radial flow is allowed; and at the edge of the inertially neutral outer vortex the flow is strictly horizontal.

For a given momentum source, $\Delta v/\tau$, (10.2) indicates that in the absence of boundaries $\partial v/\partial t$ ($r^* = r_0^*$, $z^* = 0$)$/v_{max}$ is independent of v_{max}. The increase in the vertical scale of the secondary circulation for large v_{max} (as γ^* and R^* become small) is balanced by the decreased strength of the circulation (as the inertial stability of the vortex increases). For weak storms, however, the Rossby radius is much larger than the radius of maximum wind r_m ($R^* \gg 1$). Then, the boundary condition at $r^* = 0$ becomes important. Fluid parcels are constrained to move horizontally by the relatively weak inertial stability of the vortex. The presence of the inner boundary prevents horizontal motions at $r^* = 0$ so that the response inside $r^* < r_0^*$ is reduced. In terms of the images in Fig. 3c, the response in $0 < r^* < r_0^*$ is reduced when the image of the source across $r^* = 0$ cancels the radial flow due to the source itself. Explicit calculation using (10.2) for the source at $x_0^* = \frac{1}{2}r_0^{*2}$, $z_0^* = 0.5$, and its image at $x^* = -x_0^*$, shows that the cancellation becomes effective in reducing the response at $r^* = r_0^*$ when $\gamma^* \geq 2$. $\gamma^* \geq 2$ corresponds to $v_{max} \leq 30$ m s^{-1}. For $v_{max} \geq 30$ m s^{-1}, the horizontal scale of the response is small enough that the meridional circulation in $r^* < 1$ is not significantly constrained by the central boundary. Thus, the normalized response for the momentum source is independent of v_{max} for $v_{max} \geq 50$ m s^{-1}.

The response to a fixed heat source, as for the momentum source, is reduced in $r^* < r_0^*$ when the Rossby radius of deformation is much larger than the radius of maximum wind ($R^* \gg 1$). The constraint $u = 0$ at $r^* = 0$ modifies the response for weak vortices. The transition at $r^* = 1$ between the inner and outer vortex plays a dominant role here, however. For the analytic solutions an image sink is required at r_i^* to satisfy the interface condition $w = 0$ at $r^* = 1$ (Fig. 3b). The radial scale of the

[2] Since the maximum wind tendency does not in general occur at the RMW, $(\partial v/\partial t)_{max}/v_{max}$ is not the maximum growth rate $[(\partial v/\partial t)/v]_{max}$.

response is R^*. As R^* increases, the distance between r_0^* and r_i^* decreases, when scaled by R^*. Then, the circulations due to the reflections of r_0^* and r_i^* cancel more completely, so that the magnitude of the response is reduced for weak vortices.

The numerical results (Figs. 5a and 5b and dashed lines in Figs. 4a and 4b) were extended to include more general barotropic vortices. The response to sources of heat and momentum at $r_0^* = 1$, $z_0^* = 0.5$ were evaluated with $v_{max} = 50$ m s^{-1}, as in Fig. 5. The vertical structure of the vortex was modified to include the fourfold increase in N^{*2} between the troposphere and stratosphere above $z^* = 1$. Although the response at the lid ($z_T^* = 1.5$) was considerably reduced, the response at the ground was essentially unmodified. A variable density $\rho^*(z^*)$, with constant scale height $H = 0.5Z$ was included. Due to the reduction in density at the level of forcing ($z_0^* = 0.5$), the response at the ground was reduced. The radial profile of tangential wind was changed from a quadratic to a linear profile in $r^* \leqslant 0.85$. This profile has a larger inertial stability in $0 \leqslant r^* \leqslant 0.82$ than does the quadratic. Thus the response to the momentum source, which directly forces radial motions, was reduced. Lastly, the radial profile of tangential wind was changed in $r^* \geqslant 1.15$ from the inertially neutral r^{*-1} profile to $r^{*-0.5}$. This increased the inertial stability in the outer vortex to a realistic value. Figs. 7 and 8 show the meridional circulation and surface tangential wind tendencies, with all the modifications in both the vertical and horizontal structure of the barotropic vortex described above included. The increased inertial stability in $r^* > 1$ has considerably reduced the magnitude of u in that region. The corresponding increase in the scale of the transition between the inner and outer vortex has reduced the effect of the outer vortex on the response in $r^* < 1$. The image at r_i^* for **B** in the analytic formulation (Fig. 3b) canceled the radial flow in $r^* < 1$ due to the source at r_0^*; that for **V** (Fig. 3c) reinforced it. Thus the broadening of the transition in the numerical formulation has increased the response in $r^* < 1$ for **B** (cf. Fig. 5a) and decreased it for **V** (cf. Fig. 5b). In the former case the positive gyre has been enhanced, leading to stronger $u > 0$ and $\partial v/\partial t < 0$ in $r^* < 0.7$. These quantitative changes do not alter the essential qualitative dependence of the response on the constraints imposed by the vortex geometry described previously.

The inner negative gyre in Fig. 7 is substantially weaker than the outer positive one. This arises from the combined effect of larger values of the discriminant D^* inside the eye and (to a lesser degree) of imaging across the center boundary. Within the eye, high windspeed, small radius and the cyclonic sense of the horizontal shear of v^* combine to make the local inertia frequency $(\zeta^*\xi^*)^{1/2}$, and hence D^*, large. Outside the eye decreasing wind speed, increasing radius, and anticyclonic shears result in

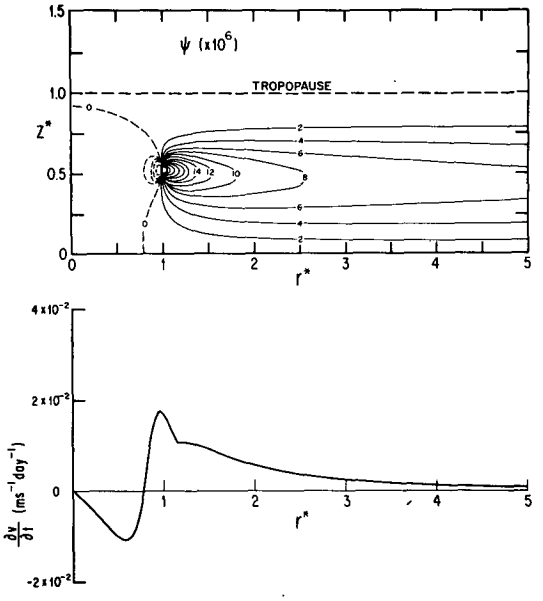

FIG. 7. Numerical solution for streamfunction and surface tangential wind tendency due to source of heat at $r^* = 1$, $z^* = 0.5$. Vortex is barotropic with variable density, stratification and tangential wind profile described in text. $v_{max} = 50$ m s^{-1}. Streamfunction contour interval is 2×10^{-6}.

smaller values for both quantities. As discussed above, when the wind speed is >30 m s^{-1} the flow near the source is not much affected by its image across the center; at lower wind speeds the image source, which acts to cancel both ψ itself and its vertical gradient, weakens the inner gyre significantly. Thus, in a weak storm both large D^* and imaging across the center reduce the inner gyre, but in a stronger storm, as shown in Fig. 7, only the former effect is important.

When allowance is made for the distortion of the axes in Fig. 7, the inner gyre has nearly the same vertical and radial extents. The outer gyre, on the other hand, extends outward to large radii. The streamfunction contours in the outer part of the positive gyre are largely horizontal, but those near the source and in the negative gyre are more steeply inclined. Although this is partly caused by the center boundary condition, it arises primarily from the radial variation of R^*. For a vortex of 50 m s^{-1}, the local inertia and buoyancy frequencies within the eye are comparable; R^* is order 1. Thus, the ratio of the vertical and radial motions also is typically of order 1. Outside the eye, the smaller inertia frequency makes $R^* \gg 1$, so radial motion predominates there. Inside the eye, the response acts to redistribute mass efficiently; outside it acts to redistribute momentum.

4. Baroclinic vortex

This section extends the previous results to baroclinic vortices with horizontal and vertical structures that more closely resemble hurricanes in nature. The

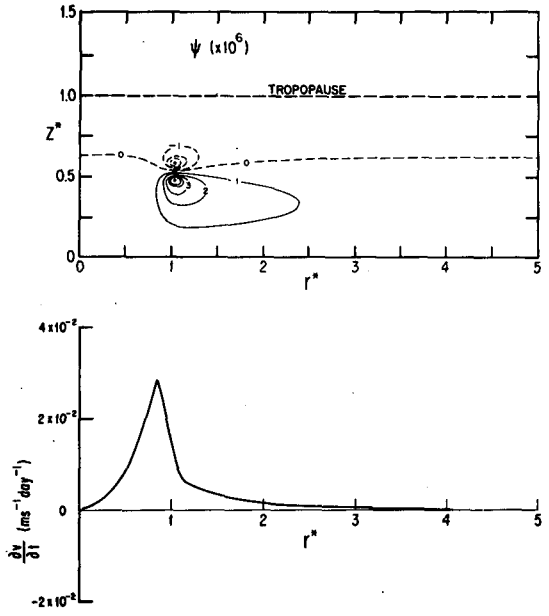

FIG. 8. As in Fig. 7 except due to momentum source. Streamfunction contour interval is 1×10^{-6}.

horizontal structures are the same as those for the realistic barotropic vortices at the end of Section 3 (cf. Figs. 7 and 8). The tangential wind profile is linear inside the eye, $r^* \leqslant 0.85$, and proportional to $r^{*-0.5}$ outside the eye, $r^* \geqslant 1.15$, with a cubic spline transition in $0.85 \leqslant r^* \leqslant 1.15$. The maximum value is $v^* = 1$ at the surface and $r^* = 1$. The vorticity is constant in $r^* \leqslant 0.85$, decreasing outward from that region. In the vertical, the wind decreases from a maximum near the surface to zero at $z^* = 1.6$, 0.1 nondimensional units above the top of the domain. The vertical shear and radial buoyancy gradients are strongest near $z^* = 0.8$. The nondimensional buoyancy frequency, N^*, takes into account both the variations in b^* required to sustain the mean vortex and the fourfold increase in stability at the tropopause. The background density is a function of height alone. Unless otherwise indicated, the results are obtained with $v_{max} = 50$ m s^{-1} at latitude 20°N, and the forcing is the same as in Section 3.

Fig. 9 shows the streamfunction and velocity fields induced by a heat source at $r^* = 1$ and $z^* = 0.25$. The qualitative character of the response is the same as that of the barotropic vortex in Fig. 7. Baroclinic effects, however, constrain the updraft jet that lies between the two gyres to slope outward along the angular momentum isolines. Although the center boundary of the vortex reduces the radial flow there to zero, it increases the vertical flow, and hence strengthens the compensating descent about the vortex axis. FC makes the case that this descent inside the eye, as well as the convergence into the eye aloft and the divergence at the surface, can be most simply explained in terms of the thermally-induced feature described here.

Fig. 10 illustrates the dimensional height tendency of a constant pressure surface, $\partial z_p/\partial t = (\partial\phi/\partial t)/g$ at $z = 0$, associated with the secondary circulation. In addition to the total dimensional tendency of height, the contributions of compensating subsidence, $-N^2w/g$, and radial advection, $-(u/g)\,\partial b/\partial r$, appear [cf. (4.4)]. Within the eye the former term is primarily responsible for the height fall, but inward advection of cool air aloft acts to reduce the fall somewhat. Outside the eye, the situation is reversed. The height fall is sustained by outward advection of warm air in the baroclinic upper troposphere. Although some compensating subsidence does occur at the same altitude as the source, it is more than balanced by net ascent at levels above and below. The

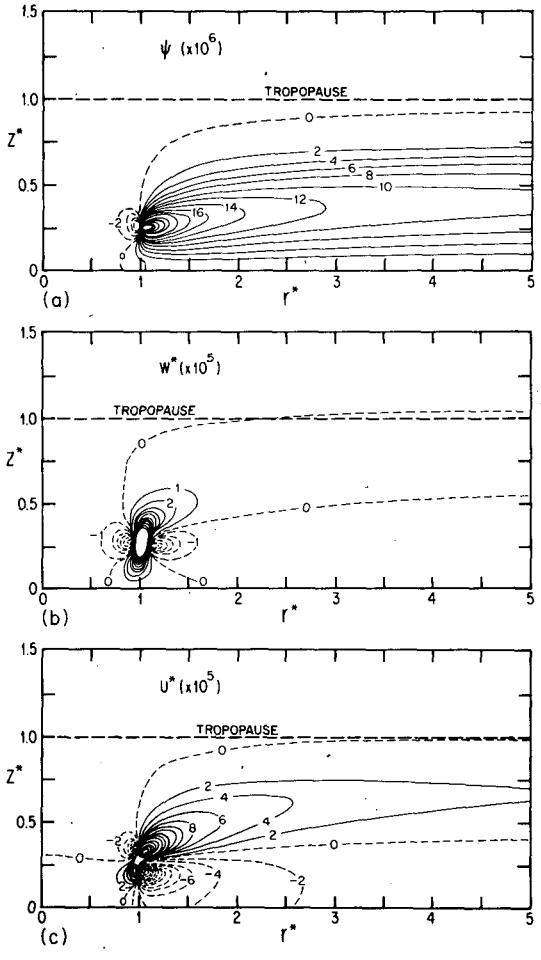

FIG. 9. The response to a heat source at $z_0^* = 0.25$ and $r_0^* = 1$ in a baroclinic vortex. The fields shown are: (a) mass-flux streamfunction with contour interval 2×10^{-6}; each contour unit (1×10^{-6}) is equivalent to 0.825 kg m^{-1} s^{-1}, (b) vertical velocity with contour interval 1×10^{-5}; each contour unit equals 5×10^{-4} m s^{-1}, (c) radial velocity with contour interval 2×10^{-5}; each unit is equivalent to 5×10^{-4} m s^{-1}.

net effect of vertical motions outside the eye thus acts to partially oppose that of warm outward advection.

For a source inside the eye, the most rapid height falls lie adjacent to the source and not at the center of the eye. The rate of height fall is slower in the center and very much slower in the outer vortex; the strongest positive radial gradient of $\partial z_p/\partial t$ lies near and inside $r^* = 1$.

The induced surface wind tendency, also shown in Fig. 10, is as expected from the pressure-height tendency and the gradient wind relation. Outside the eye the gradual increase in $\partial z_p/\partial t$ as one moves outward from the eye leads to a slow acceleration of v. Between $r^* = 0.78$ and the center the radial gradient of $\partial z_p/\partial t$ is reversed so that the wind decelerates in the inner part of the eye. For the given source position, the maximum $\partial v/\partial t$ lies at the RMW. This happens because the surface inflow decreases rapidly to zero radially inward from the source. The pattern of wind tendencies will tend to make the maximum of v at the RMW sharper as v increases for $r^* \geqslant 1$ and decreases for $r^* < 0.8$.

Additional examples of the velocity and geopotential tendencies induced by heat sources appear in Fig. 11. All of these sources are at $z_0^* = 0.5$; they lie at radii $r_0^* = 0.75$, 1.0, 1.5 and 2. For the source at $r_0^* = 1.0$, the negative gyre never reaches the surface, so the velocity tendency is positive at all radii. For

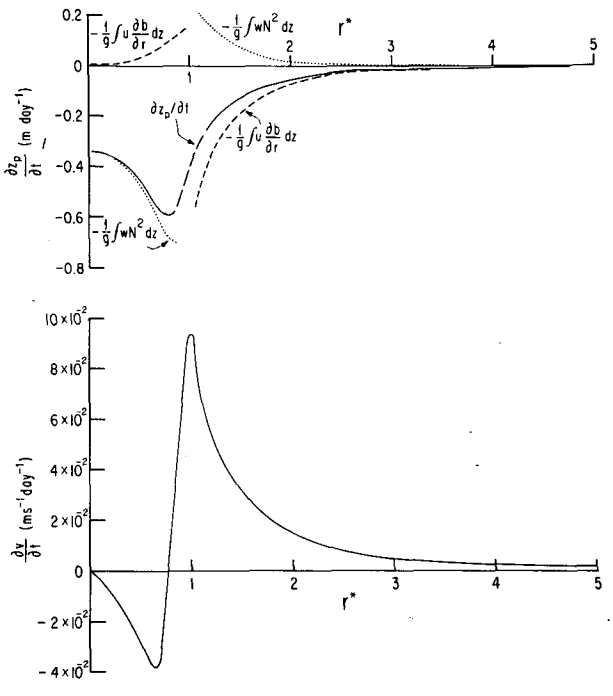

FIG. 10. The dimensional surface tendencies of pressure height and tangential wind induced by the secondary circulation shown in Fig. 9. The contributions to the pressure-height tendency of compensating subsidence and radial advection appear also.

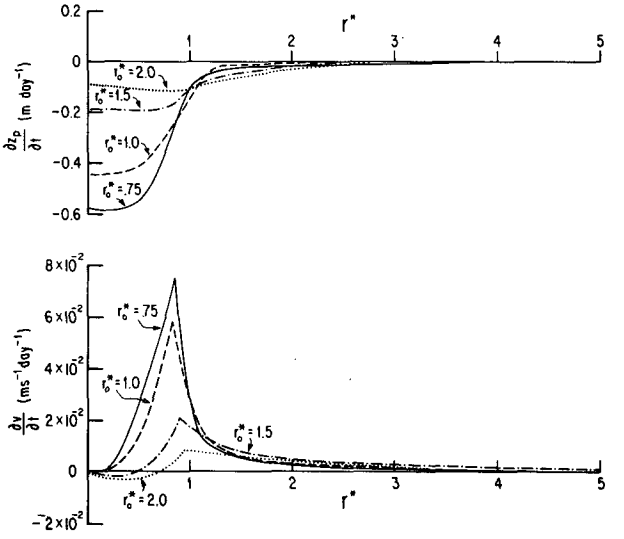

FIG. 11. The surface tendencies of pressure height and tangential wind produced by heat sources at $z_0^* = 0.5$ and $r_0^* = 0.75$, 1.0, 1.5 and 2.0.

all other source radii, the negative gyre produces outflow and weak negative velocity tendencies near the center. In the case of $r_0^* = 0.75$ this effect occurs because the motions are largely vertical; when $r_0^* \geqslant 1.5$ it happens because there is a greater horizontal distance over which the sloping boundary of the negative gyre can reach the surface. Regardless of the source's location, the greatest positive tendency is always near $r^* = 0.85$, where the strong inflow first reaches the high-vorticity core of the storm. This result is typical of all but low-level sources located just at the RMW. The radial angular momentum gradient is stronger inside the RMW rather than at the RMW, so unless u has a sharp peak at $r^* = 1$ the maximum radial advection lies within the RMW. As the maximum of v sharpens, it will tend to overtake the point of maximum increase and so limit the contraction of the RMW. Outside the RMW, the radial gradient of angular momentum is too weak to sustain large tendencies; inside, the secondary flow is more vertical and cannot advect much angular momentum radially. The location of the wind tendency peak inside the eye for most sources means that the RMW will usually tend to contract in response to convective heating that results in intensification. If the source is at or outside the RMW, the outward slope of the boundary between the gyres is crucial to this phenomenon, because it enables the inflow to penetrate the high-vorticity core. This baroclinic effect results in a significant increase in the response over the barotropic case.

The difference between the wind tendency curve in Fig. 10 and that for the $r_0^* = 1$ source in Fig. 11 illustrates another important qualitative difference between low- and high-level sources. For a source

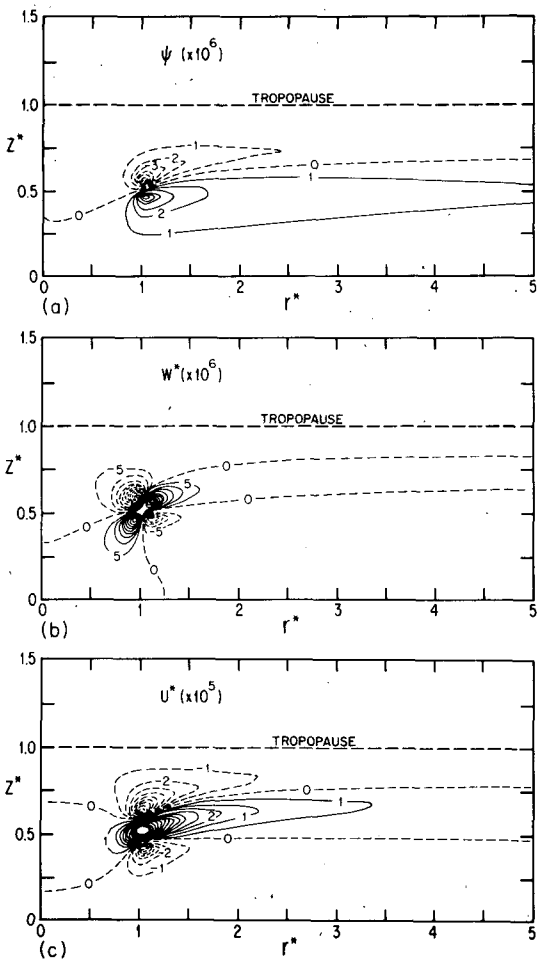

FIG. 12. The response to a momentum source at $z_0^* = 0.5$ and $r_0^* = 1$. The fields are (a) streamfunction with contour interval 1 $\times 10^{-6}$, (b) vertical velocity with contour interval 5×10^{-6}, and (c) radial velocity with contour interval 1×10^{-5}. Dimensional equivalents are the same as in Fig. 9.

near the center and above the midtroposphere, the boundary between the two gyres usually intersects the vortex center before it reaches the surface. Thus, the velocity tendencies are positive at all radii. If the source is lower—or farther from the center—the boundary intersects the ground before it reaches the axis, negative tendencies surround the center, and the profile of v inside the eye tends to become concave upward.

Fig. 12 shows the flow patterns induced by a momentum source at $r_0^* = 1$ and $z_0^* = 0.5$. In contrast with the response to heating, momentum forcing leads to outflow at the source and compensating inflow above and below. This is reflected by the presence of a positive streamfunction gyre below the source and a negative one above. The boundary between the gyres slopes upward along the isentropes. Weak descent fills most of the domain outside the source radius, with ascent confined to the sloping outflow jet between the gyres. The adiabatic temperature changes due to ascent and descent in the eye would cancel except for the stronger vertical velocities aloft caused by the decrease in background density with height. As Fig. 13 shows, this net subsidence does produce large pressure height falls inside the source radius. The effects of horizontal motion nearly cancel inside the eye. Outside, however, outward advection of warm air produces small pressure-height falls despite some cooling caused by net ascent in this part of the domain.

The velocity tendency curve for this case is qualitatively similar to that produced by a heat source. The most rapid acceleration of the tangential wind lies just inside the RMW where the radial gradient of $\partial z_p/\partial t$, and thus the horizontal angular momentum advection, is largest.

The effects of changes in the horizontal location of the momentum source at $z_0^* = 0.5$ are shown in Fig. 14. Whether the source is inside or outside the eye, the largest accelerations lie just inside the RMW, as in the heating case. Only when the source is at $r_0^* = 2$ do negative wind tendencies reach the ground. Although the source's altitude is a factor here, the extent of the positive tendencies is primarily a result of the nearly horizontal orientation of the boundary between the gyres.

Fig. 15 illustrates several experiments with heat sources at $r^* = 2$ and $z^* = 0.35$. The dimensional altitude of these sources is 5.25 km, or as close to the 0°C isotherm as the grid spacing would allow. This altitude was chosen in an effort to evaluate the direct initial effect of artificially induced latent heat release on the development of the vortex. In all three cases, the response is quite different from that discussed earlier. The boundary between the gyres

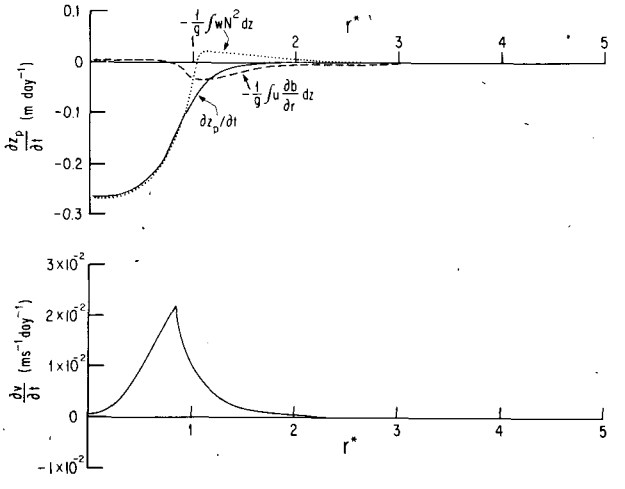

FIG. 13. The surface tendencies of pressure-height and tangential wind induced by the secondary circulation shown in Fig. 12. The contributions to the pressure-height tendency are as in Fig. 10.

reaches the ground near the RMW and negative tendencies fill the most of the eye. The strongest positive tendencies lie not in the eye wall, but either between the RMW and the source or at the source itself. If this pattern of tendencies were to persist for some time, the eye would expand and the wind profile outside the eye would flatten. Eventually, a second maximum would form near the source radius and surrounding the original eye. Depending on the exact location and nature of the source the tendency at the RMW may be either negative or weakly positive. Thus, although the maximum wind generally decreases as the eye expands it may increase slowly. Observed tendency patterns bear a close resemblance to those described above (Willoughby *et al.*, 1981).

The solid curves in Fig. 15 represent a control case in which the positive and negative elements of the heating dipole are separated by the minimum possible interval, $\delta r_0^* = 2\Delta r^* = 0.1$. This is the same configuration used in the earlier calculations. In this control, as previously, the exponent in the outer vortex is $n = \frac{1}{2}$. The dashed curves differ from the control in that the separation of the dipole is increased to $\delta r_0^* = 5\Delta r^* = 0.25$, with the total heating (and hence total dipole moment of the source) kept constant. The increased size of the dipole increases the magnitudes of the tendencies by 20–30%, but keeps the slopes of the curves nearly the same. At large radii the curves converge. This arises because the forcing is not an ideal dipole but induces significant near-field effects. As the size of the dipole increases so do the near-field effects.

The dotted curves in Fig. 15 show the result of a decrease in n, the exponent of the wind profile outside the eye, from ½ to ¼. This reduces the magnitude

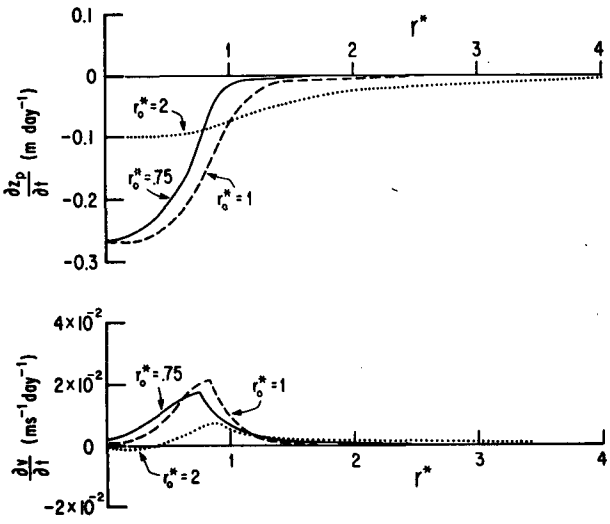

FIG. 14. The surface tendencies of pressure-height and tangential wind induced by momentum sources at $z_0^* = 0.5$ and $r_0^* = 0.75$, 1.0 and 2.0.

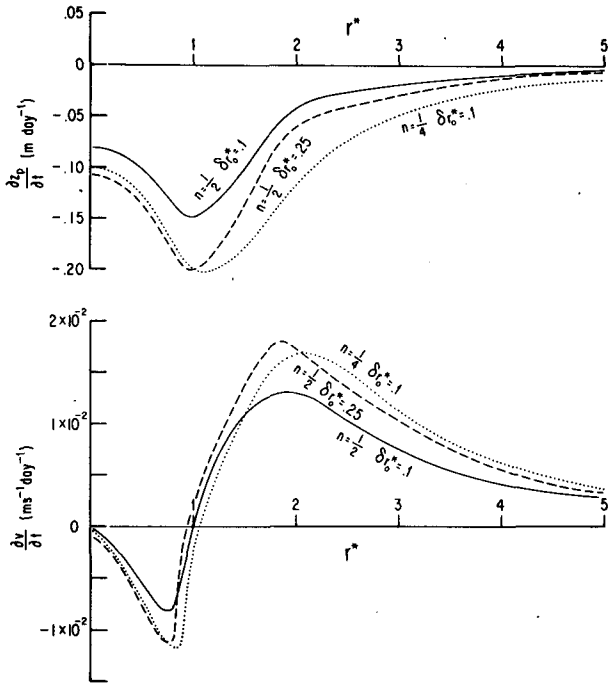

FIG. 15. The surface tendencies of pressure-height and tangential wind induced by heat sources at $z_0^* = 0.35$ and $r_0^* = 2.0$. The solid curves are a control case in which the heat source fills only two grid cells and the exponent in the tangential wind profile is $n = \frac{1}{2}$. The dashed curves show the result of a 2.5-fold increase in the diameter of the heat source with the total heat input kept constant. The dotted curves show the result of changing n to ¼ using the same heat source as in the control.

of the anticyclonic shear and results in a 50% increase in vorticity. The compensating subsidence is more confined near source, so the most rapid increase in v is both larger and closer to the source. The induced radial winds are weaker because of greater inertial resistance, but the larger radial angular momentum gradient more than compensates, so the wind tendencies increase. If the same change in vortex structure is applied with the source located in the eye or the eye wall, virtually no change results. This happens because the large inertial stability surrounding the source constrains the response too strongly for changes in the outer vortex to have much effect.

The effect of changes in R^* is further illustrated in Fig. 16, which is analogous to Fig. 6 but is computed using the realistic, baroclinic vortex structure. The maximum normalized tendency of the tangential wind is shown at differing values of v_{max} for constant heat sources at $z_0^* = 0.5$, $r_0^* = 1$ and 2, as well as for a constant momentum source at $z_0^* = 0.5$, $r_0^* = 1$. The values of R^* at the surface and $r^* = 1$ also appear; R^* at $r^* = 2$ is about three times the value at $r^* = 1$. The curves for sources at the RMW may be compared with those for the analytic solutions in Fig. 6. The magnitude of the response to the heat source is much greater for the baroclinic case than

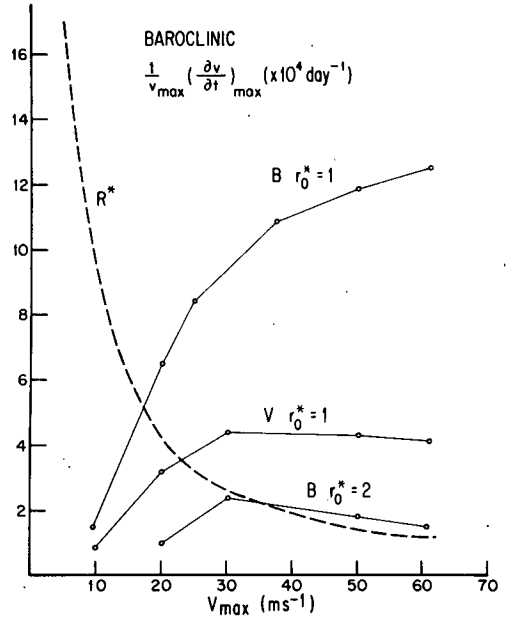

FIG. 16. Normalized tendency of surface tangential wind ($\times 10^4$ day^{-1}) for baroclinic vortices of different strengths. Response to heat source (**B**) at $z_0^* = 0.5$, $r_0^* = 1$ and 2, and to momentum source (**V**) at $z_0^* = 0.5$, $r_0^* = 1$ are shown. The dashed line shows the local nondimensional Rossby radius of deformation at the RMW.

for the barotropic, as explained in the discussion of Fig. 11. The shapes of the corresponding curves for both heat and momentum are strikingly similar. In both cases, the rate of intensification for weaker vortices ($v_{max} < 35$ m s^{-1}) is much less than for stronger ones. The roles of the central boundary and low inertial stability in the outer vortex in reducing the response for weak storms were emphasized in Section 3.

The variation of the response to a heat source at $r_0^* = 2$ in Fig. 16, however, is different from the eyewall case. The response is much weaker because of the separation between the source and the strong angular momentum gradient of the vortex core. The growth rate actually decreases slightly when $v_{max} > 35$ m s^{-1}. This is because increasing wind speed decreases R^*, so that the inner gyre's horizontal extent is reduced and the flow at the edge of the vortex core is weaker. The radial profiles of induced velocity tendency in this case resemble those in Fig. 15 rather than Fig. 10. The largest $\partial v/\partial t$ tends to lie near the source and not near the RMW.

5. Summary and discussion

This paper has treated the Green's function response of a symmetric hurricane-like vortex to point heat or momentum sources. Eliassen (1951) found that three factors control the character of such induced transverse circulations: thermodynamic stability, baroclinity and inertial stability. The first of these is sensibly constant, but the others increase with the intensity of the vortex. Baroclinity acts to incline the axis of the flow so that near a heat source the response tends to follow a constant angular momentum surface, and near a momentum source the response tends to follow an isentrope.

Much of the present analysis depends on the control of the response's horizontal extent by inertial stability. In the scaling of Section 2 the nondimensional response is found to be independent of the dimensional horizontal scale of the vortex; however, R^*, the nondimensional horizontal scale of the response defined by (7), decreases as the maximum windspeed increases. Indeed, the maximum windspeed is the only significant parameter of the nondimensional symmetric response to a fixed forcing.

A heat source forces a transverse circulation with ascent through the source itself and compensating subsidence in the surroundings. In nature, the updraft is observed to have a horizontal scale of ~5 km. The dimensional equivalent of R^* may vary from several hundred kilometers in a weak system to ten kilometers in an intense hurricane. In the latter case $R^* \sim 1$, so there is no pronounced scale separation between the updraft and subsidence—both of which have roughly the same horizontal scale as the eye.

Section 3 treats the combined effect of lateral boundary conditions and variations in R^* on the induced transverse circulations in barotropic vortices. At the central axis, symmetry requires no horizontal flow. The flow becomes increasingly horizontal outward from the RMW, where the inertial stability is relatively weak. For a source near the RMW both these effects may significantly modify the response. In a weak storm, where the horizontal scale of the response is much greater than the RMW (i.e., $R^* \gg 1$), the flow is blocked by the central axis and extends to large radius where the resistance to horizontal motion is relatively small. Both these effects reduce the horizontal flow, and thus the rate of change of the surface tangential wind, between the source and the axis. On the other hand, in strong vortices ($v_{max} \geq 35$ m s^{-1}) increased inertial resistance lessens both effects. In this situation, when $R^* \leq 2$, the source produces a local recirculation inside the RMW that is not influenced by its image across the vortex axis. The compensating subsidence due to a heat source will tend to warm and dry the region inside the RMW, but will not affect the convective heating across the center of the vortex. This acts to suppress convection inside the RMW and form a visible eye. It is not coincidental that the local recirculation occurs when $v_{max} \geq 35$ m s^{-1}, the stage of development when the characteristic hurricane eye forms.

Smith (1981) has recently used simple single- and multi-layered models to diagnose the adjustment of

a symmetric balanced vortex to a local removal or vertical redistribution of mass and angular momentum. The depth of his one-layer model is $h = 5.5$ km. The radial profile of tangential wind is the same as that for the realistic barotropic vortex at the end of Section 3. For a vortex strength $v_{max} = 40$ m s^{-1} and a mass sink—equivalent to a heat source—near the RMW ($r_0 \approx r_m$), Smith diagnoses values of both u and $\partial v/\partial t$ in $r < r_0$ several orders of magnitude smaller than those in $r > r_0$ (Smith's Fig. 4). This result is not consistent with the substantial values of $\partial v/\partial t$ inside $r < r_0$ diagnosed in the present analyses (cf. Figs. 7, 10, 11). The source in Smith's one-layer model is uniformly distributed in the vertical, while that in our continuously stratified model is a point source. Thus direct comparison of the results is difficult. An important part of the difference between the results may be explained, however, in terms of differences in gravitational stability and the influence of the central boundary when R^* is large. For the one-layer "shallow-water" model, the buoyancy frequency $\nu_g = (g/h)^{1/2} = 4.2 \times 10^{-2}$ s^{-1} with Smith's choice of $h = 5.5$ km. This is about four times the value $\nu_g = N = 1.0 \times 10^{-2}$ s^{-1} used in the present continuously stratified model. The large vertical stability of Smith's model increases both $(D^*)^{1/2}$ and R^* by a factor of 4. The increase in D^* reduces strength of the response. Using Smith's value of h, and $v_{max} = 40$ m s^{-1}, $R^* \approx 8$ (and $\gamma^* \approx 6$). The flow is thus constrained to be nearly horizontal. The constraint of no flow across the vortex axis together with the large vertical resistance prevents air from being drawn from $r < r_0$. Relatively more air flows inward from $r > r_0$ so that the response in $r < r_0$ is considerably reduced. If a rigid lid were put on the one-layer model so that *no* vertical motion were possible, then *all* the air would be drawn from $r > r_0$ and the response in $r < r_0$ would be identically zero. Thus, the significantly smaller response found by Smith (1981) in $r < r_0$ compared to that found in our analysis may be largely due to the much greater vertical stability used in his analysis. This conclusion illustrates the importance of the interaction of the transverse circulation with the central boundary of the vortex when $R^* \gg 1$.

Section 4 extends the results to baroclinic vortices with realistic horizontal and vertical structures. For a heat source near the RMW the baroclinically-induced inward slope of the boundary between the streamfunction gyres allows the inflow to extend inside the radius of the source and to penetrate the high-vorticity core of the vortex. This behavior considerably increases the maximum wind tendency relative to that of the same source in the barotropic vortex. For both heat and momentum sources near the RMW, the greatest positive wind tendencies usually lie within the eye adjacent to the RMW and so act to constrict and intensify the wind maximum. In the absence of other physical processes, the radial profile of v would develop a sharp peak near the maximum of $\partial v/\partial t$. The continued inward movement of the RMW depends on processes that maintain both the heat and momentum sources and the rounded profile of v near the RMW. These processes, including boundary-layer frictional convergence and internal diffusion, are not included in this analysis. All the tendencies diagnosed in this paper are based on a specified profile of v and may not, by themselves, be used to predict the long-term evolution of the vortex. The intensifying effect of the momentum sources illustrates a mechanism for hurricane development involving eddy momentum fluxes that has been emphasized recently by Challa and Pfeffer (1980).

Lower tropospheric heat sources, and heat or momentum sources at somewhat larger radius, induce negative velocity tendencies near the center of the eye. This tends to make the wind profile across the eye U shaped. Sources at still larger radii extend the negative tendencies to, or even beyond, the RMW. This mechanism may explain how outer concentric eye walls replace a preexisting inner eye. Current strategies for the amelioration of hurricanes (Gentry, 1969) seek to induce this behavior artificially, which has been numerically simulated in that context (Rosenthal, 1971).

Several examples of the above phenomena have been observed in hurricanes and are described in Willoughby *et al.* (1982, this issue). In that paper, the present model is used to diagnose the response to a distributed heat source that simulates the action of the eye wall of Hurricane Allen of 1980. The diagnosed radial profiles of both wind and pressure tendencies closely resemble those computed from aircraft measurements in the hurricane itself.

The magnitude of the response to the specified heat source (10°C day^{-1} in a 0.75×0.75 km cell) is small, with maximum normalized wind tendency $\sim 10^{-3}$ day^{-1} for $v_{max} = 50$ m s^{-1}. Assuming a cloud mass flux detrainment rate of 0.75 day^{-1}, a cloud-environment temperature difference of 4°C, and a distribution of heating over an area 5 km deep $\times$ 45 km radius, the normalized tendency due to the total heating converts to about 0.12 day^{-1}. If momentum rates are adjusted in an equivalent manner, accounting for detrainment of momentum in the baroclinic atmosphere, the rate of intensification due to the total momentum source also converts to $\sim$0.12 day^{-1}. Thus, the total normalized wind tendency due to both heat and momentum sources is $\sim$0.24 day^{-1}. Horizontal velocity increments convert to realistic values of several meters per second. Although this analysis is crude, it does indicate that the magnitudes of the responses presented are reasonable and that heat and momentum sources may contribute equally to the intensification process.

The tendencies presented here are instantaneous

rates. As the vortex develops, the structure of the storm will be modified. In particular, changes in frictional convergence in the boundary layer will change the convection, thus modifying the heat and momentum sources as well as the evolution of the storm. Balanced prognostic models (Ooyama, 1969; Sundqvist, 1970) include this feedback, but the present work does not. Thus, the results in this paper should not in themselves be used to infer the ultimate evolution of a hurricane vortex after the addition of heat. They do, however, indicate the effects of scale interactions on the response to heat and momentum sources that are relevant for modified or unmodified hurricane-like vortices.

Acknowledgments. The authors thank Drs. K. V. Ooyama and S. Lord for many valuable comments on an earlier version of this paper. We are grateful to Ms. Angel Tillman and Mr. Dale Martin for their expert help with the manuscript and illustrations.

REFERENCES

Challa, M., and R. Pfeffer, 1980: Effects of eddy fluxes of angular momentum on model hurricane development. *J. Atmos. Sci.*, **37,** 1603–1618.

Eliassen, A., 1951: Slow thermally or frictionally controlled meridional circulation in a circular vortex. *Astrophys. Norv.*, **5,** 19–60.

Gentry, R. C., 1969: Project STORMFURY. *Bull. Amer. Meteor. Soc.*, **50,** 404–409.

Holton, J., 1975: *The Dynamic Meteorology of the Stratosphere and Mesosphere.* Amer. Meteor. Soc., 216 pp.

Ooyama, K., 1966: On the stability of the baroclinic circular vortex: a sufficient criterion for instability. *J. Atmos. Sci.*, **23,** 43–53.

——, 1969: Numerical simulation of the life-cycle of tropical cyclones. *J. Atmos. Sci.*, **26,** 3–40.

Rosenthal, S., 1971: A circularly symmetric primitive-equation model of tropical cyclones and its response to artificial enhancement of the convective heating functions. *Mon. Wea. Rev.*, **99,** 414–426.

Smith, R. K., 1981: The cyclostropic adjustment of vortices with application to tropical cyclone modification. *J. Atmos. Sci.*, **38,** 2021–2030.

Sundqvist, H., 1970: Numerical simulation of the development of tropical cyclones with a ten-level model, I. *Tellus*, **22,** 359–390.

Willoughby, H. E., 1978: A possible mechanism for the formation of hurricane rainbands. *J. Atmos. Sci.*, **35,** 838–848.

——, 1979: Forced secondary circulations in hurricanes. *J. Geophys. Res.*, **84,** 3173–3183.

——, J. A. Clos and M. G. Shoreibah, 1982: Concentric eye walls, secondary wind maxima and the evolution of the hurricane vortex. *J. Atmos. Sci.*, **39,** 395–411.